machines

MDPI

Article

Structural Parameter Effects on Flow Stability and Classification Performance in a Turbo Air Classifier

Weifeng Qian and Yun Zeng *

Institute for Strength and Vibration of Mechanical Structures, Yangtze University, Jingzhou 434023, China; 201973037@yangtzeu.edu.cn

* Correspondence: 520053@yangtzeu.edu.cn; Tel.: +86-13617267033

Abstract

Understanding which structural parameters govern flow stability and particle separation is essential for turbo air classifier design. In this study, the Y160L-6 turbo air classifier was used to examine whether different categories of spatial structural parameters influence classification performance through the same flow mechanism or play distinct roles in regulating the internal flow field. Two representative parameters, namely the spacing between the secondary air inlet and the rotor cage and the spacing between the secondary air inlet and the feed inlet, were analyzed using computational fluid dynamics (CFD) coupled with the RNG k–ε turbulence model and the discrete phase model (DPM). The results show that the two parameters affect the classifier through different mechanisms. Increasing the secondary air inlet–rotor cage spacing causes a non-monotonic variation in wall pressure and tangential velocity, indicating a strong influence on the global swirling structure. At a spacing of 1490 mm, the pressure distribution in the classification zone becomes more uniform, the tangential velocity reaches a relatively high level, and the intensity of the precessing vortex core (PVC) is reduced. Under this condition, the cumulative proportion of 2–5 μm particles at the fine powder outlet increases by 34.1% compared with the initial configuration. In contrast, variations in the secondary air inlet–feed inlet spacing exert only a limited influence on the overall flow structure and classification characteristics under relatively low feed inlet velocity conditions, indicating that this parameter mainly affects local flow disturbance rather than global flow stability. These findings demonstrate that structural parameters associated with the coupling between secondary airflow and rotor rotation dominate classifier performance, whereas parameters related to feed–air interaction exert only a secondary effect under low feed momentum conditions. These findings provide design guidance for the investigated Y160L-6 turbo air classifier and may serve as a reference for similar classifier structures under comparable operating conditions.

Keywords: turbo pneumatic classifier; fluent; precessing vortex core; flow field characteristics; classification characteristics

Check for updates

Academic Editor: Pedro Javier Gamez-Montero

Received: 1 June 2026
Revised: 30 June 2026
Accepted: 30 June 2026
Published: 8 July 2026

Copyright: © 2026 by the authors. Licensee MDPI, Basel, Switzerland. This article is an open access article distributed under the terms and conditions of the Creative Commons Attribution (CC BY) license.

1. Introduction

Turbo air classifiers are widely used in powder processing industries because of their high classification efficiency and flexible cut-size adjustment capability. Their separation performance is governed by the complex interaction between swirling airflow, centrifugal effects, and particle transport behavior. As a result, the internal flow field plays a decisive role in determining classification sharpness, fine particle recovery, and overall process stability [1–3].

With the development of computational fluid dynamics (CFD), numerical simulation has become an effective approach for investigating gas–solid flow behavior in turbo air classifiers. Previous studies have shown that geometric parameters such as rotor cage configuration, blade number, installation angle, and inlet layout can significantly influence internal flow structure and classification performance [4–7]. These studies have confirmed that structural modification is an effective way to improve classifier operation. However, most existing work has focused on the optimization of individual components or local geometric details, while less attention has been paid to the different physical roles played by distinct types of spatial arrangement parameters [8–10].

Previous studies on turbo air classifiers have mainly focused on the influence of rotor cage structure, guide vanes, blade geometry, inlet layout, and operating parameters on classification performance. These studies have shown that changes in local structural components can affect the cut size, separation sharpness, pressure distribution, and particle residence time. Recent investigations have also indicated that fine powder separation is limited not only by the nominal cut size, but also by the stability and uniformity of the internal swirling flow and the transport behavior of fine particles [11].

Flow-induced stability is a common concern in rotating machinery, where leakage flow, swirling motion, and fluid–structure interaction may affect equipment performance and operational reliability [12]. In turbo air classifiers, the strongly swirling flow is often accompanied by unstable vortex structures, including the precessing vortex core (PVC), which may induce pressure fluctuation, flow distortion, and deterioration of classification stability. Therefore, understanding how structural parameters affect flow stability is not only important for design optimization, but also essential for clarifying the mechanism by which geometry regulates particle separation [13].

For the Y160L-6 turbo air classifier considered in this study, the feed inlet and secondary air inlet are arranged asymmetrically, and the fine powder outlet is eccentrically distributed. This geometry leads to two different types of structural interactions within the classifier. The first is the coupling between the secondary airflow and the rotor cage, which is expected to directly influence the global swirling structure. The second is the interaction between the secondary airflow and the feed inlet flow, which is more likely to affect local vortex formation near the inlet region. Although both interactions are associated with structural arrangement, their effects on flow stability and classification behavior may be fundamentally different [14,15].

Although previous studies have improved the understanding of structural optimization in turbo air classifiers, most of them have focused on individual component optimization. The distinct roles of different categories of spatial structural parameters have not been sufficiently clarified. In particular, it remains unclear whether parameters associated with secondary airflow–rotor coupling dominate global swirling flow stability, and whether parameters associated with feed–air interaction mainly affect local flow disturbance. Clarifying this difference is important for identifying the dominant structural parameter and improving classifier design.

Accordingly, the central research question of this study is as follows: in a turbo air classifier, which type of spatial structural parameter predominantly governs global flow stability and particle classification performance, and through what flow mechanism does this control occur? To address this question, two representative structural parameters were selected in the Y160L-6 turbo air classifier: the spacing between the secondary air inlet and the rotor cage, and the spacing between the secondary air inlet and the feed inlet. By comparing their effects on pressure distribution, tangential velocity, particle trajectories, and fine particle recovery using CFD coupled with the RNG $k-\varepsilon$ model and

the discrete phase model (DPM), this study aims to distinguish the different physical roles of global-flow-regulating and local-disturbance-related structural parameters [16].

The results are expected to provide not only an optimized structural configuration for the studied classifier, but also a clearer physical insight into how different structural parameters regulate swirling flow stability and particle separation in turbo air classifiers.

2. Theory and Method

2.1. Working Principle of Turbo Air Classifier

The vertical classification system, as shown in Figure 1, mainly comprises a turbine air classifier, cyclone separators, and a collection device. Figure 1a shows the overall schematic diagram of the classification equipment. After grinding, the material enters the classification chamber through the feed inlet and subsequently enters the impeller zone via gravitational settling and secondary airflow entrainment. The separation mechanism of a turbo air classifier is primarily governed by the balance among centrifugal force, aerodynamic drag force, and gravity acting on particles within a rotating flow field [17]. Particles with larger diameters are subjected to greater centrifugal forces and are discharged as coarse products, whereas fine particles are entrained by the airflow and conveyed to the fine powder outlet.



(**a**) (**b**)

Figure 1. Scheme diagram of the pneumatic screening system. (**a**) Overall view of the classification equipment; (**b**) Prototype of a turbine air classifer.

The material sequentially passes through a vibrating elevator and a vibrating mill to reduce it to a specified fineness. Large particles first undergo preliminary separation in the gravity settling chamber, followed by subsequent classification through a cascade of parallel-and series-connected cyclone separators and the turbine air classifier. Finally, the classified materials are collected by a bag collector. Figure 1b illustrates the structure of the turbine air classifier.

The structural dimensions of the Y160L-6 turbo air classifier are illustrated in Figure 2. Particles enter the interior of the classifier together with airflow through the feed inlet, while the secondary air inlet provides an additional airflow that entrains the particles and guides them upward into the classifier impeller. Particles of different diameters are separated under the action of centrifugal force generated by the rotating impeller. Within the flow field, particles are simultaneously subjected to centrifugal force, aerodynamic drag, and gravity. Particles with larger diameters experience centrifugal force exceeding aerodynamic drag, causing them to migrate toward the outer region of the classifier, impact the wall, and be discharged from the coarse powder outlet under the action of gravity.

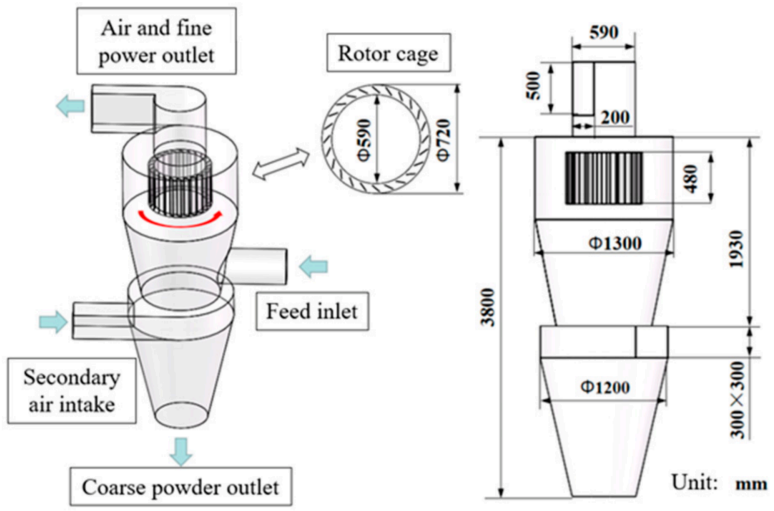


Figure 2. Turbo air classifier structure.

The Y160L-6 turbo air classifier exhibits structural asymmetry in its internal flow field, including asymmetric arrangements of the feed inlet and secondary air inlet, as well as an eccentrically distributed fine powder outlet. This asymmetry can induce instability in the tangential airflow velocity and consequently deteriorate classification efficiency. Therefore, suppressing or mitigating the precessing vortex core (PVC) phenomenon within the flow field is a key issue for improving the classification performance of turbo air classifiers.

From the perspective of particle separation, the motion of particles in the classifier is determined by the competition between centrifugal force and aerodynamic drag. For a particle moving in the rotating flow field, the centrifugal tendency increases with particle size and tangential velocity, whereas the aerodynamic drag tends to entrain fine particles toward the fine powder outlet. Therefore, the stability of the tangential velocity field and the radial pressure gradient directly affect the separation path of particles. A more stable swirling flow is beneficial for maintaining a consistent force balance, reducing random particle dispersion, and improving classification sharpness.

After particles enter the classifier through the feed inlet, the airflow supplied by the secondary air inlet entrains the particles and transports them into the grading impeller. The flow field between the secondary air inlet and the rotor cage is highly complex and characterized by vortex core structures, while additional local vortices form in the region between the secondary air inlet and the feed inlet. These flow phenomena can induce instability in the internal flow field of the classifier, thereby directly affecting its classification performance. Therefore, representative structural parameters—including the distance between the secondary air inlet and the rotor cage, as well as the distance between the secondary air inlet and the feed inlet—were selected to investigate their effects on flow field characteristics and classification behavior of the turbo air classifier. Based on this analysis, the structural parameters of the classifier were further optimized.

2.2. Mathematical Model

2.2.1. Turbulence Model

The gas-phase flow was modeled using the Reynolds-averaged Navier–Stokes (RANS) equations coupled with the RNG $k-\varepsilon$ turbulence model. This model is suitable for strongly swirling and high-strain-rate turbulent flows and has been widely applied in turbo air classifier simulations [13].

The transport equations for turbulent kinetic energy k and its dissipation rate ε are expressed as:

$$\partial(\rho k)/\partial t + \partial(\rho k u_i)/\partial x_i = \partial\left[(\mu + (\mu/\sigma_k))(\partial k/\partial x_j)\right]/\partial x_j + G_k - \rho\varepsilon \quad (1)$$

$$\partial(\rho\varepsilon)/\partial t + \partial(\rho\varepsilon u_i)/\partial x_j = \partial\left[(\mu + (\mu_t/\sigma_\varepsilon))(\partial\varepsilon/\partial x_j)\right]/\partial x_j - C_{1\varepsilon}(\varepsilon/k)G_k - C_{2\varepsilon}\rho\left(\varepsilon^2/k\right) - R \quad (2)$$

where $\mu_t = \rho C_\mu\left(k^2/\varepsilon\right)$ is the turbulent viscosity, where μ is the molecular viscosity, ρ is the fluid density, and u_i is the velocity component in the i-direction.

G_k represents the production of turbulent kinetic energy, and R is the additional term in the RNG $k-\varepsilon$ turbulence model accounting for the effect of swirl.

C_μ = 0.0845
$C_{1\epsilon}$ = 1.42
$C_{2\varepsilon}$ = 1.68
σ_k = 1.0
σ_ε = 1.3

2.2.2. Particle Motion Model

Particle trajectories were calculated using the discrete phase model (DPM) under the dilute phase assumption. Under the present operating conditions, the particle concentration is relatively low; therefore, particle–particle interactions were neglected [18–20].

The particle motion is governed by Newton's second law:

$$du_p/dt = F_D(u - u_p) + g(\rho_p - \rho)/\rho_p + F_{other} \quad (3)$$

The drag force per unit particle mass is defined as:

$$F_D = \frac{18\mu}{\rho_p d_p^2}\frac{C_D \mathrm{Re}_p}{24} \quad (4)$$

where:
u_p and u are particle and fluid velocities;
ρ_p is particle density;
d_p is particle diameter;
C_D is drag coefficient;
Re_p is particle Reynolds number;
g is gravitational acceleration.

Because the particle concentration is low, virtual mass and particle–particle interaction forces are neglected. Considering the small particle size (mean diameter ≈ 6 μm), the Saffman lift force is included, while Brownian motion is neglected due to its relatively weak contribution under the present flow conditions.

2.3. Simulation Settings

A hybrid mesh was generated to discretize the computational domain. Tetrahedral elements were applied in complex rotating regions, while structured hexahedral elements were used in regular flow passages [7]. The final mesh consisted of approximately 7.9×10^5 cells. The mesh configuration is shown in Figure 3.

A multiple reference frame (MRF) approach was adopted to model rotor rotation. The rotor cage region was defined as a rotating zone with a rotational speed of 800 rpm, while the remaining domain was treated as stationary. The main numerical simulation settings and boundary conditions are summarized in Table 1.

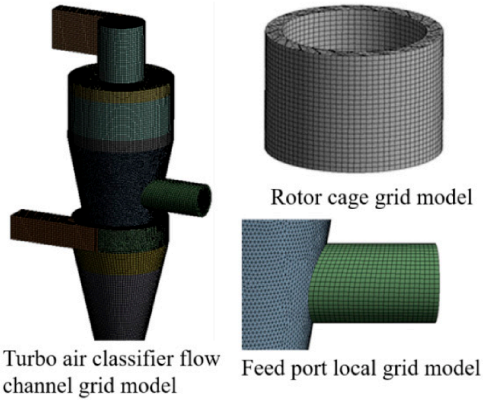


Figure 3. Turbo air classifier flow channel grid model.

Table 1. Numerical simulation settings and boundary conditions.

Item	Setting
Gas phase	Air
Air density	1.293 kg/m^3
Turbulence model	RNG k–ε
Particle model	DPM
Rotor speed	800 rpm
Feed inlet	Velocity inlet, 5 m/s
Secondary air inlet	Velocity inlet, 12 m/s
Outlet	Pressure outlet
Pressure–velocity coupling	SIMPLEC
Spatial discretization	Second-order upwind
Convergence criterion	Residuals below 1×10^{-4}
Mesh size	7.9×10^5 cells

Pressure–velocity coupling was handled using the SIMPLEC algorithm. A second-order upwind discretization scheme was applied, and convergence was assumed when residuals dropped below 1×10^{-4}.

2.4. Mesh Independence Verification

To ensure that the numerical results were not significantly affected by mesh resolution, a mesh independence verification was conducted under the representative secondary air inlet–rotor cage spacing of 1490 mm. Three mesh levels were generated, namely a coarse mesh with 5.20×10^5 cells, a medium mesh with 7.90×10^5 cells, and a fine mesh with 1.12×10^6 cells. The maximum wall pressure, peak tangential velocity, and the proportion of 2–5 μm particles at the fine powder outlet were selected as evaluation indicators.

As shown in Table 2, the differences between the medium mesh and the fine mesh are small. Compared with the fine mesh, the relative deviations in the medium mesh are 0.26% for maximum wall pressure, 0.30% for peak tangential velocity, and 0.28% for the proportion of 2–5 μm particles. In contrast, the coarse mesh shows larger deviations for all three indicators. Therefore, the medium mesh with approximately 7.90×10^5 cells was adopted in this study, considering both numerical accuracy and computational efficiency. The convergence trend of the 2–5 μm particle proportion with increasing mesh number is shown Figure 4. The data points represent the calculated results under different mesh levels, and the connecting line is used only to indicate the variation trend.

Table 2. Mesh independence verification under the representative setting 1490 mm secondary air inlet–rotor cage spacing condition.

Mesh Level	Number of Cells	Maximum Wall Pressure (Pa)	Peak Tangential Velocity (m/s)	Proportion of 2–5 μm Particles (%)
Coarse mesh	5.20×10^5	976.6	26.42	62.55
Medium mesh	7.90×10^5	994.46	27	63.90
Fine mesh	1.12×10^6	997.1	27.08	64.08

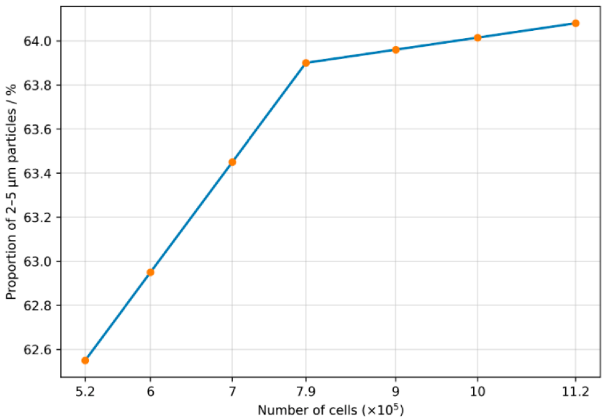


Figure 4. Mesh independence verification based on the proportion of 2–5 μm particles at the fine powder outlet. The markers represent the simulated values at different mesh levels, and the connecting line indicates the variation trend.

3. Influence of the Spacing Between the Secondary Air Inlet and the Rotor Cage

In a turbo air classifier, suppressing or attenuating the vortex core within the flow field is an effective approach for enhancing flow field stability. The formation of strong rotating vortices is primarily attributed to the coupled interaction between the secondary air inlet airflow and the rotor cage rotation. Consequently, the distance between the secondary air inlet and the rotor cage is a critical structural parameter governing flow field evolution and classification behavior.

To verify this hypothesis, this study varies the distance between the rotor cage center and the upper edge of the secondary air inlet, as illustrated in Figure 5 (corresponding to the initial 1390 mm reference dimension). The influence of different secondary air inlet–rotor cage spacing on flow field characteristics and classification performance of the turbo air classifier was systematically investigated. The parameter variation process was classified into two stages: coarse adjustment and fine adjustment. Using a hierarchical parameter selection strategy, seven spacing values—1390 mm, 1440 mm, 1465 mm, 1477.5 mm, 1490 mm, 1512.5 mm, and 1515 mm—were ultimately selected as fine parameters for analyzing the effects of secondary air inlet–rotor cage distance.

The secondary air inlet–rotor cage spacing can be regarded as a global-flow-regulating structural parameter because it directly determines the interaction distance between the secondary inlet jet and the rotor-induced swirling flow. When this spacing changes, the development of the annular swirling region, the radial pressure gradient, and the intensity of the vortex core are simultaneously affected. Therefore, this parameter is expected to have a stronger influence on global flow stability than parameters located farther from the rotor cage.

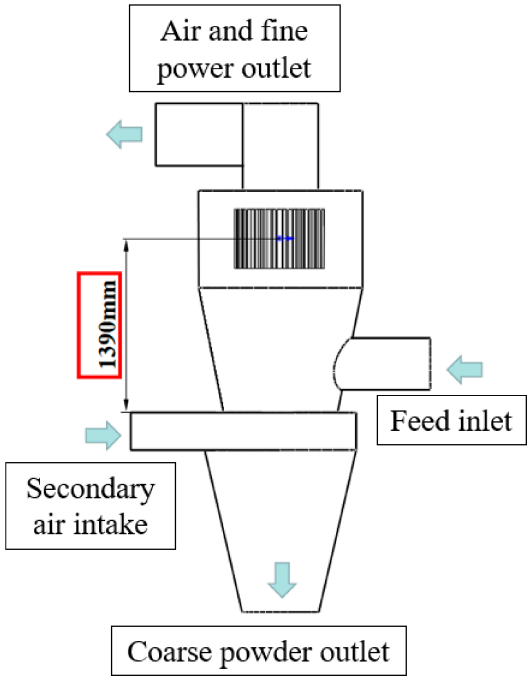


Figure 5. Distance between the secondary air inlet and the rotor cage of the turbo classifier. The red box indicates the initial secondary air inlet-rotor cage spacing of 1390 mm.

3.1. Pressure Distribution Under Different Secondary Sir Inlet-Rotor Cage Spacings

Figure 6 presents the pressure contour maps on the horizontal plane (Z = 0) and vertical plane (X = 0) under different secondary air inlet–rotor cage spacings. The pressure variation along the intersection line of these two sections is also plotted.

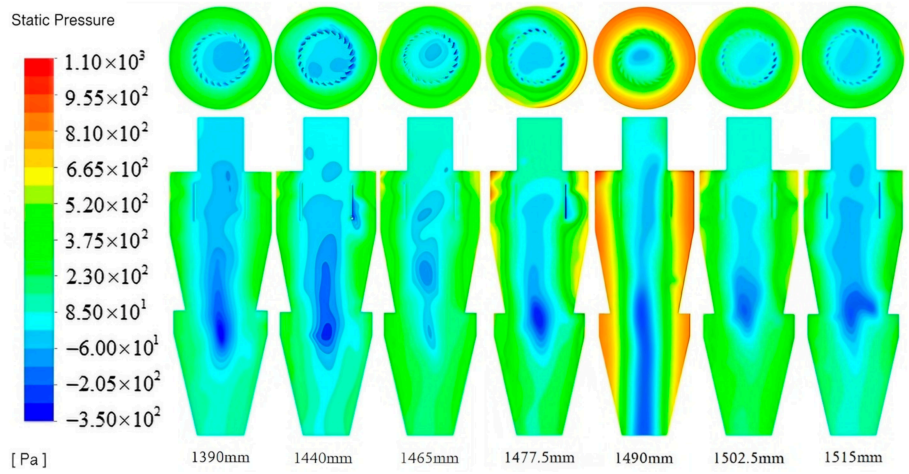


Figure 6. Contour plots of pressure distribution in the flow field of a classifier with different distance from the secondary air inlet to the rotor cage.

As the spacing increases from 1390 mm to 1515 mm, the internal pressure field exhibits a non-monotonic variation. The diameter of the central negative-pressure region first decreases and then expands, while the maximum wall pressure increases initially and subsequently declines.

When the spacing reaches 1490 mm, the pressure distribution within the classification zone becomes more uniform. A relatively high pressure is observed near the outer wall, whereas lower pressure is maintained along the rotor cage axis. This pressure gradient enhances radial force balance and contributes to improved flow stability. At this spacing,

the intensity of the precessing vortex core (PVC) is observed to weaken, as reflected by the smoother pressure distribution and reduced axial pressure distortion.

This indicates that the 1490 mm spacing provides a more favorable development distance for the secondary inlet jet before it interacts with the rotor-induced swirling flow. When the spacing is too small, the secondary airflow enters the rotor-influenced region before a stable annular flow structure is sufficiently developed. When the spacing is too large, the annular region expands excessively and local turbulence is intensified. In contrast, the 1490 mm spacing promotes a more stable radial pressure gradient and reduces the distortion of the central low-pressure core.

Quantitative analysis (Figure 7) shows that the wall pressure reaches a maximum value of 994.46 Pa at 1490 mm, representing an increase of 465.15 Pa compared with the initial configuration (1390 mm). The enhanced pressure difference between the classification zone and the fine powder outlet strengthens the centripetal drag force acting on particles. When the drag force becomes sufficiently dominant over centrifugal force for small particles, separation efficiency is improved.

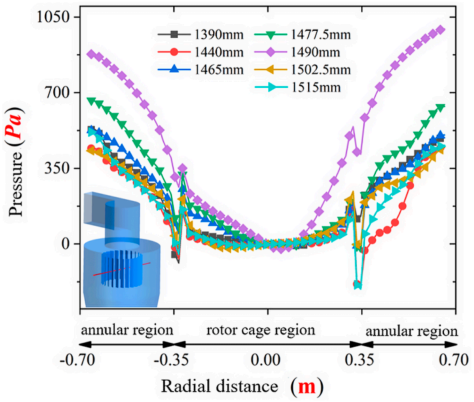


Figure 7. Pressure distribution curves under different distances from the secondary air inlet-rotor cage spacing. Each colored curve corresponds to a spacing value shown in the legend.

3.2. Tangential Velocity Distribution

Figure 8 shows the tangential velocity contour maps under different secondary air inlet-rotor cage spacing, and Figure 9 presents the corresponding velocity profiles along the section intersection line.

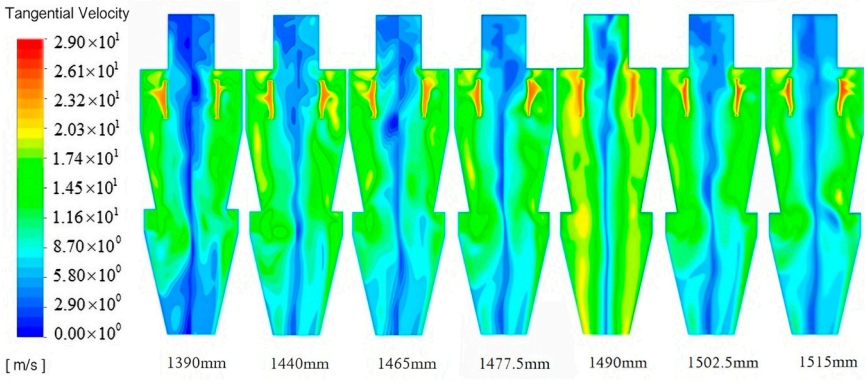


Figure 8. Contour plots of tangential velocity distribution under different distances from secondary air inlet to rotor cage.

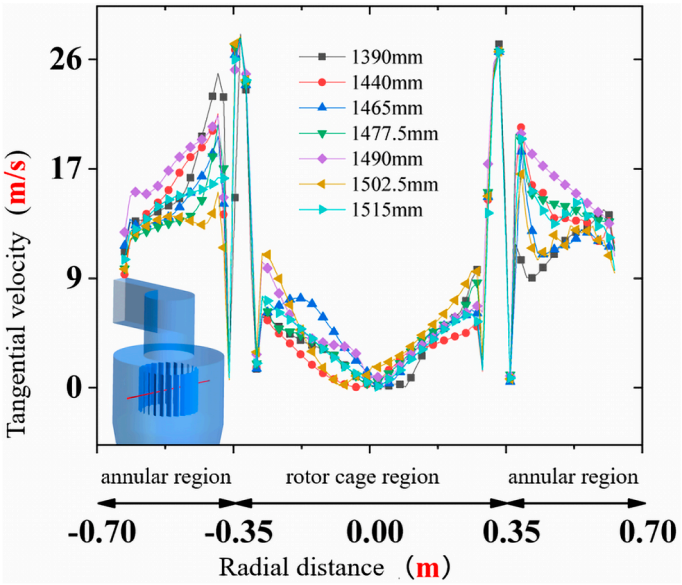


Figure 9. Tangential velocity distribution curve of the flow field in the classifier with different distances from the secondary air inlet to the rotor cage.

The tangential velocity distribution follows a trend consistent with the pressure variation, exhibiting an initial increase and subsequent decrease as spacing increases. The maximum tangential velocity, approximately 27 m/s, occurs near the rotor blades.

It should be noted that relatively large fluctuations appear at the beginning of the velocity profile in the annular region. These fluctuations are mainly attributed to the interaction between the secondary inlet jet and the rotating flow generated by the rotor cage. In this region, the airflow experiences strong shear and local recirculation, leading to rapid variations in tangential velocity along the sampling line. The mesh independence test and convergence monitoring indicate that the main velocity distribution is not significantly altered by further mesh refinement. Therefore, these fluctuations are mainly considered to be associated with local physical flow disturbances rather than numerical instability.

At 1490 mm spacing, tangential velocity in both the primary and secondary conical regions reaches a relatively high and uniform level. Although variations in tangential velocity within the classification zone remain within 3 m/s across different configurations, the overall flow field uniformity is improved at this spacing.

Since centrifugal force depends on tangential velocity, the limited variation in velocity within the classification zone implies that centrifugal force changes are relatively small. Therefore, the improvement in classification performance is mainly attributed to the enhanced pressure difference and resulting drag force, rather than a substantial increase in centrifugal force.

3.3. Particle Trajectories and Classification Performance

For most configurations, particle residence time remains within 2 s. However, at 1490 mm spacing, a larger proportion of 4 μm particles exits through the fine powder outlet, while fewer particles are discharged as coarse product. Particle trajectories appear smoother and less chaotic, indicating improved flow stability.

Figure 10 illustrates the trajectories of 4 μm particles under different secondary air inlet-rotor cage spacings. Figure 11 shows the particle size distribution at the fine powder outlet, and Figure 12 presents the corresponding cumulative distribution curves.

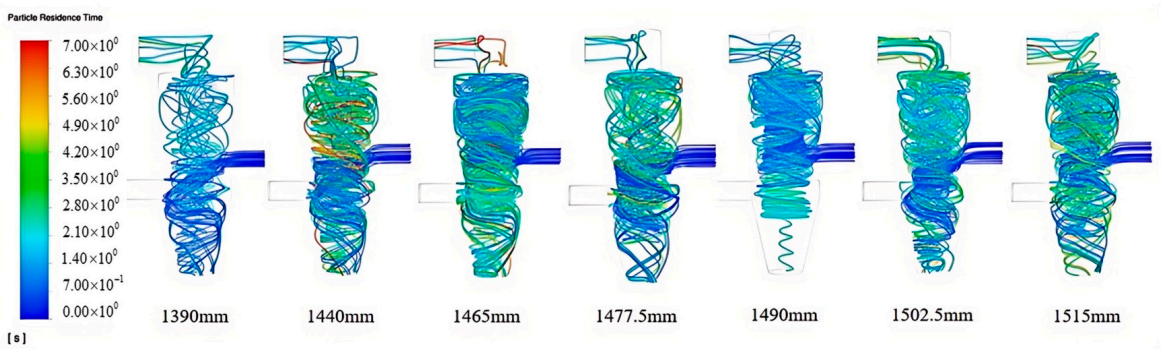


Figure 10. Trajectories of 4 μm particles in the classifier under different secondary air inlet–rotor cage spacings.

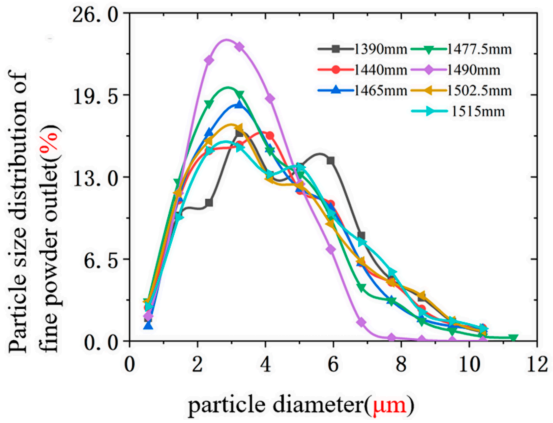


Figure 11. Particle size distribution curve at the outlet of fine powder.

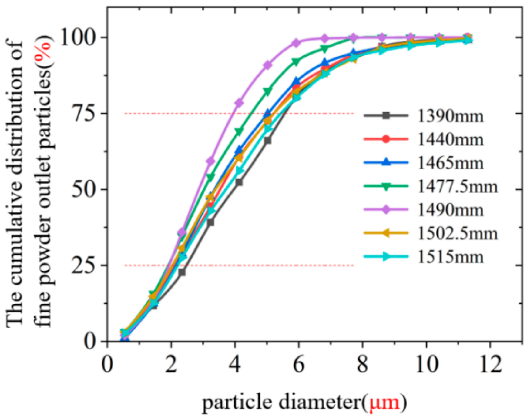


Figure 12. Accumulated distribution curve at the outlet of fine powder. The dashed horizontal reference lines are used to indicate cumulative particle proportions.

At 1490 mm spacing, the particle size distribution becomes narrower, with particles primarily concentrated in the 2–5 μm range. Quantitative analysis reveals that particles within this size interval account for 63.9% of the total particle number at the fine outlet. Compared with the initial 1390 mm configuration, the proportion of 2–5 μm particles increases by 34.1%.

This improvement confirms that classification performance is maximized at 1490 mm spacing. The observed non-monotonic behavior indicates that excessive spacing enlarges the annular region and intensifies internal turbulence, thereby weakening separation efficiency.

4. Influence of the Spacing Between the Secondary Air Inlet and the Feed Inlet

As illustrated in Figure 13, the secondary air inlet and feed inlet of the turbo air classifier investigated in this study are not centrally symmetrical. This asymmetric design is intended to utilize opposing airflow directions between the feed inlet and the secondary air inlet, thereby promoting air convection to disperse agglomerated particles at the feed inlet. However, the interaction between these two inlet airflows can induce local vortical structures within the classifier, thereby affecting the stability of the internal flow field.

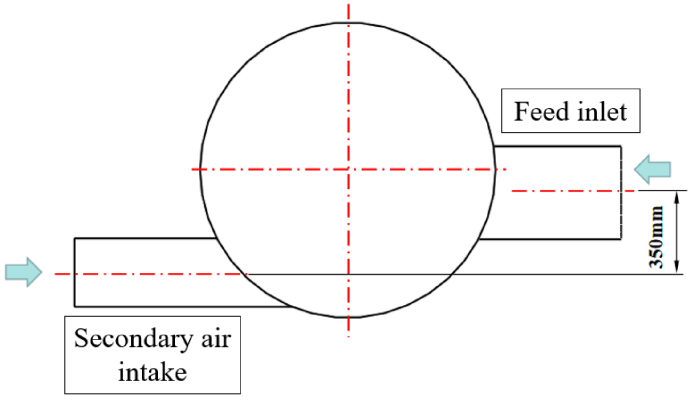


Figure 13. Distance between the secondary air inlet and feed inlet of the turbo air classifier.

Compared with the secondary air inlet–rotor cage spacing, the secondary air inlet–feed inlet spacing is more closely related to local inlet interaction. Since this parameter does not directly change the relative position between the secondary airflow and the rotor cage, its influence on the global swirling structure is expected to be weaker. Under the present low feed inlet velocity condition, the feed airflow has limited momentum and mainly affects local vortex displacement near the inlet region.

To investigate this effect, this study adjusts the distance between the secondary air inlet and the feed inlet while maintaining the feed inlet position fixed and varying only the location of the secondary air inlet. The reference distance parameter of 350 mm shown in Figure 13 is modified to examine the influence of different secondary air inlet–feed inlet spacings on the flow field characteristics and classification performance of the turbo air classifier. The parameter variation process was classified into two stages: coarse adjustment and fine adjustment. Using a hierarchical parameter selection strategy, seven spacing values—150 mm, 250 mm, 350 mm, 450 mm, 550 mm, 650 mm, and 750 mm—were ultimately selected for analysis.

4.1. Pressure Distribution Characteristics

Figure 14 presents the pressure contour maps on the horizontal plane (Z = 0) and vertical plane (X = 0) for different secondary air inlet–feed inlet spacings. The pressure variation along the section intersection line is shown in Figure 15.

Unlike the spacing between the secondary air inlet and the rotor cage, variations in the secondary air inlet–feed inlet distance exert only limited influence on the overall pressure distribution within the classifier. The axial negative-pressure region remains nearly unchanged across different spacing configurations, and no significant variation in PVC-related pressure distortion is observed.

A localized negative-pressure region appears near the junction of the primary and secondary conical sections, corresponding to the interaction zone between the secondary airflow and the feed inlet airflow. As the spacing increases, this local vortex shifts laterally; however, its intensity does not exhibit substantial change.

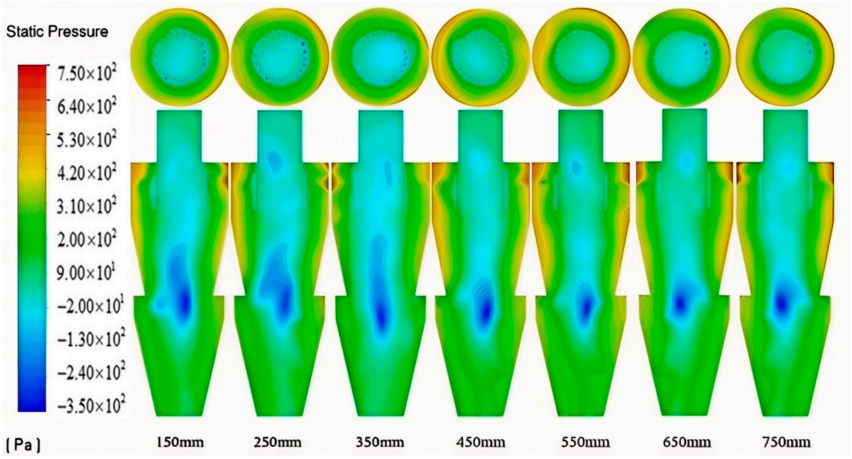


Figure 14. Contour plots of pressure distribution in the flow field of the classifier under different secondary air inlet–feed inlet spacings.

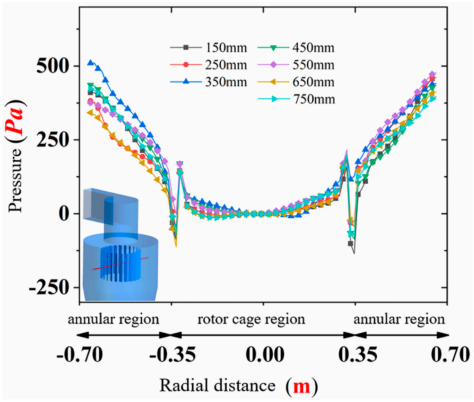


Figure 15. Pressure distribution curve of the classifier flow field under different secondary air inlet–feed inlet spacings.

This behavior can be attributed to the relatively low velocity at the feed inlet compared with the secondary air inlet. The weaker feed airflow lacks sufficient momentum to significantly modify the dominant swirling structure generated by the rotor cage and secondary airflow. Consequently, global pressure distribution and flow stability remain largely unaffected.

This result further indicates that the secondary air inlet–feed inlet spacing mainly changes the location of local flow interaction, but does not significantly modify the rotor–dominated global pressure structure.

4.2. Tangential Velocity Characteristics

Figure 16 shows the tangential velocity contour maps, and Figure 17 presents the corresponding velocity profiles along the section intersection line.

Consistent with the pressure distribution results, the tangential velocity field exhibits only minor variations as the secondary air inlet–feed inlet spacing increases. The dominant swirling motion in the classification zone remains stable, and no pronounced changes in peak tangential velocity are observed.

Although slight fluctuations appear due to local vortex displacement and inherent PVC-induced instability, these variations are considerably smaller than those observed in Section 3 when adjusting the secondary air inlet–rotor cage distance.

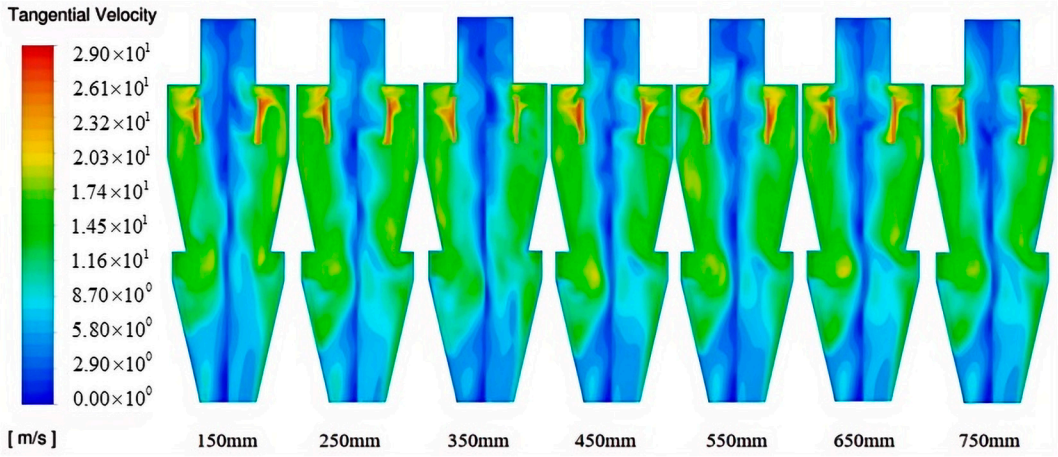


Figure 16. The tangential velocity distribution cloud diagram of different secondary air inlets to the feed inlet distance of the classifier.

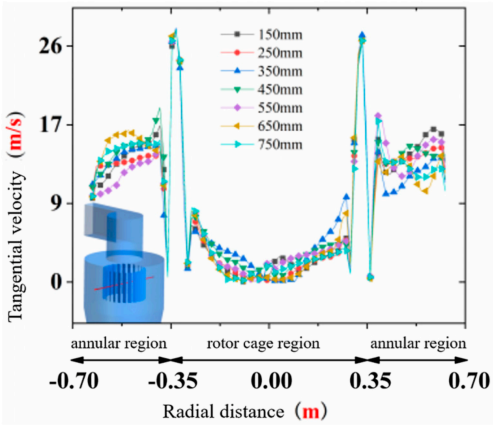


Figure 17. Contour plots of tangential velocity distribution in the flow field of the classifier at different distance from the secondary air inlet to the feed inlet.

Therefore, under the present operating condition (feed inlet velocity = 5 m/s), the structural adjustment of the secondary air inlet relative to the feed inlet does not substantially alter the global tangential velocity distribution.

The weak variation in tangential velocity confirms that the dominant swirling motion is controlled primarily by the rotor cage and secondary airflow coupling rather than by the feed inlet position.

4.3. Particle Trajectories and Classification Performance Under Different Secondary Air Inlet-Feed Inlet Spacings

Figure 18 illustrates the trajectories of 4 μm particles for different secondary air inlet–feed inlet spacings. The color scale indicates particle residence time.

Across all configurations, particle trajectories exhibit similar patterns, and residence times remain within a comparable range. The number of particles exiting through the fine powder outlet shows minimal variation.

Figure 19 presents the particle size distribution at the fine powder outlet, while Figure 20 shows the cumulative distribution curves. Although minor differences are observed in particle distribution among the different spacing configurations, the overall trends are highly consistent. All cases exhibit multi-peak characteristics, and the proportion of particles within the 2–5 μm range remains nearly unchanged.

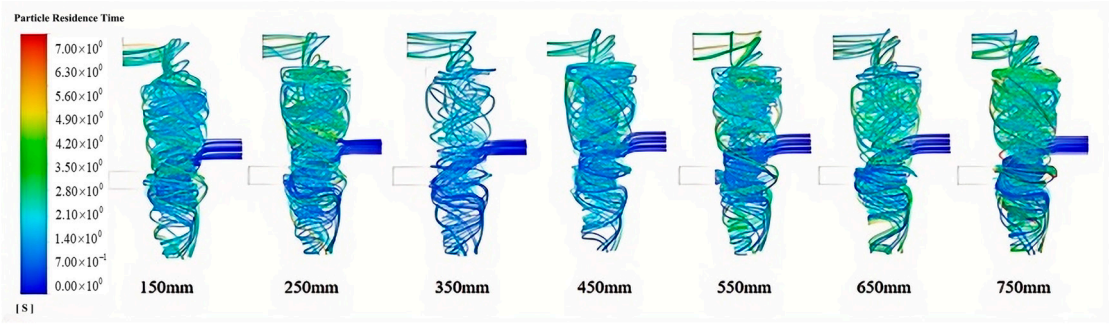


Figure 18. Trajectory of 4 μm particles in the classifier under different secondary air inlet–feed inlet spacings.

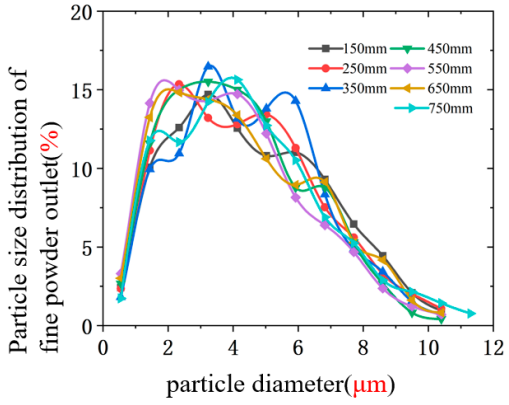


Figure 19. Particle size distribution at the outlet of fine powder.

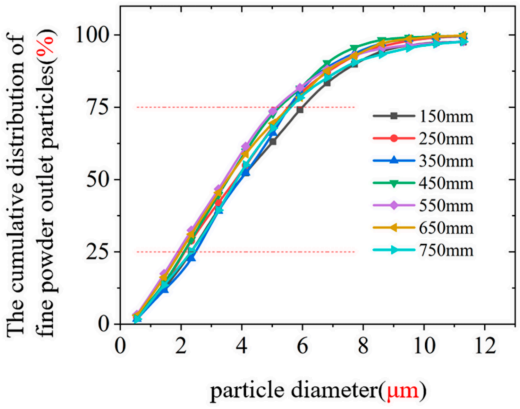


Figure 20. Accumulated particle distribution at the outlet of fine powder. The dashed horizontal reference lines are used to indicate cumulative particle proportions.

Compared with the pronounced non-monotonic behavior observed when varying the secondary air inlet–rotor cage distance, the influence of the secondary air inlet–feed inlet spacing on classification performance is negligible under the current low feed velocity condition.

This indicates that, when the feed airflow momentum is insufficient to significantly disturb the dominant swirling structure, spatial adjustment of the feed inlet relative to the secondary air inlet does not effectively modify flow stability or separation efficiency.

Therefore, the nearly unchanged particle size distribution can be attributed to the limited influence of feed-related spacing on global flow stability. This finding supports the conclusion that feed–inlet related spacing acts as a local–disturbance-related parameter under the investigated operating conditions.

5. Conclusions

This study systematically investigated the influence of two structural parameters—the spacing between the secondary air inlet and the rotor cage, and the spacing between the secondary air inlet and the feed inlet—on the internal flow field and classification performance of a Y160L-6 turbo air classifier using CFD coupled with the RNG $k-\varepsilon$ model and DPM. The main conclusions are summarized as follows:

1. Increasing the secondary air inlet–rotor cage spacing results in a non-monotonic variation in flow field characteristics and classification performance. Wall pressure and tangential velocity first increase and then decrease as the spacing enlarges. When the spacing reaches 1490 mm, the pressure distribution becomes more uniform, the intensity of the PVC–pressure distortion is reduced, and the drag–centrifugal force balance is optimized. Under this condition, classification performance is maximized, with the cumulative proportion of 2–5 μm particles at the fine powder outlet reaching 63.9%, representing a 34.1% increase compared with the initial configuration.
2. In contrast, variations in the secondary air inlet–feed inlet spacing exert only limited influence on global pressure distribution, tangential velocity structure, and particle classification behavior under the present low feed inlet velocity condition. Although local vortices shift position with spacing adjustment, their intensity remains relatively unchanged and does not significantly modify the dominant swirling structure. Consequently, classification performance remains nearly constant across different spacing values.
3. Overall, the results demonstrate that structural parameters affecting the coupling between secondary airflow and rotor cage rotation play a dominant role in regulating flow stability and separation efficiency, whereas parameters associated with feed inlet positioning have a comparatively minor effect under low inlet velocity conditions. These findings provide useful guidance for the structural optimization and performance enhancement of turbo air classifiers.

It should be noted that this study is based on numerical simulations, and direct experimental validation was not performed in the present work. Although mesh independence and convergence analyses were conducted to improve the reliability of the numerical results, experimental measurements of the internal flow field and classification performance will be necessary in future work to further validate the predicted trends.

Author Contributions: W.Q.: Conceptualization, Methodology, Numerical simulation, Formal analysis, Data curation, Visualization, Writing—original draft. Y.Z.: Conceptualization, Supervision, Writing—review and editing, Funding acquisition. All authors have read and agreed to the published version of the manuscript.

Funding: This work was supported by the Petro China Science and Technology Innovation Fund. (No. 2024DQ02-0307), the Hubei Provincial Science and Technology Plan Project (No. 2025EIA094), and the Open Fund of the Key Laboratory of Fluid and Power Machinery, Ministry of Education (No. LTDL/2023013).

Data Availability Statement: The original contributions presented in this study are included in the article. Further inquiries can be directed to the corresponding author.

Conflicts of Interest: The authors declare that they have no known competing financial interests or personal relationships that could have appeared to influence the work reported in this paper.

References

1. Diao, X. Study on Pre-Dispersion and Application of Particles in Ultrafine Classifier. Master's Thesis, Southwest University of Science and Technology, Mianyang, China, 2013.

2. Lu, D.; Tang, Z.; Fan, Y.; Lu, C. Performance of large-difference-particle air classifier. *CIESC J.* **2021**, *72*, 4184–4195.
3. Zhang, Y. Study on Classification Mechanism and Equipment Design of SCX Ultrafine Separator. Master's Thesis, Southwest University of Science and Technology, Mianyang, China, 2010.
4. Yang, Y. Numerical Simulation of Two-Phase Flow and Structural Design Research in Powder Mineral Separation. Master's Thesis, Kunming University of Science and Technology, Kunming, China, 2021.
5. Yu, Y.; Chen, W.; Kong, X.; Ren, C.; Liu, J. Design of the new guide vane for the turbo air classifier. *Mater. Werkst.* **2023**, *54*, 196–206. [CrossRef]
6. Qin, X.; Zhang, J.; Tang, C.; Tang, M. Turbine classifier impeller flow field analysis and structural optimization. *Coal Min. Mach.* **2023**, *44*, 142–145.
7. Karunakumari, L.; Eswaraiah, C.; Jayanti, S.; Narayanan, S.S. Experimental and numerical study of a rotating wheel air classifier. *AIChE J.* **2005**, *51*, 776–790. [CrossRef]
8. Ren, W.; Liu, J.; Yu, Y. Design of rotating cage with arc blades in eddy current air classifier. *J. Mech. Eng.* **2016**, *52*, 195–201.
9. Yang, Q.; Liu, J. Internal flow field analysis and rotor cage structure improvement of vortex air classifier. *Chem. Eng.* **2010**, *38*, 79–83.
10. Zhang, Y. Flow Field Simulation Analysis and Inlet Layout Optimization of Vortex Air Classifier. Master's Thesis, Beijing University of Chemical Technology, Beijing, China, 2022.
11. Abohelwa, M.; Benker, B.; Javadi, M.; Wollmann, A.; Weber, A.P. Limitation in the Performance of Fine Powder Separation in a Turbo Air Classifier. *Processes* **2023**, *11*, 2817. [CrossRef]
12. Zhou, W.; Su, H.; Liu, H.; Zhang, Y.; Qiu, N.; Gao, B. Leakage and Rotordynamic Performance of a Semi-Y Labyrinth Seal Structure for Centrifugal Pump Based on Multifrequency Whirl Method. *J. Eng. Gas Turbines Power* **2025**, *147*, 101022. [CrossRef]
13. Yu, Y.; Ren, W.; Liu, J. A new volute design method for the turbo air classifier. *Powder Technol.* **2019**, *348*, 65–69. [CrossRef]
14. Liu, H.; Wu, W.; Tian, Y. Pressure drop analysis and flow field simulation of turbine air classifier. *Pet. Mach.* **2019**, *47*, 95–100.
15. Liu, H.; Yang, F.; Tan, H.; Li, Z.; Feng, P.; Du, Y. Experimental and numerical investigation on the structure characteristics of vortex generators affecting particle agglomeration. *Powder Technol.* **2020**, *362*, 805–816. [CrossRef]
16. Liang, L. Flow Field Diagnosis and Regulation of Eddy Current Air Classifier Based on Entropy Production Theory. Master's Thesis, Hebei University of Science and Technology, Shijiazhuang, China, 2021.
17. Liu, B.; Sun, G. Analysis and comparative Study of flow field simulation results of different turbulence models in centrifugal pneumatic classifier. *Fertil. Des.* **2023**, *61*, 8–11+44.
18. Sun, Z.; Liu, C.; Yang, G.; Chen, L. Orthogonal vortices characteristic, performance evaluation and classification mechanism of a horizontal classifier with three rotor cages. *Powder Technol.* **2022**, *404*, 117438. [CrossRef]
19. Wu, S. Mathematical Simulation of Particle Separation Process of Vortex Air Classifier and Design of Double-Layer Spreader. Master's Thesis, Beijing University of Chemical Technology, Beijing, China, 2017.
20. Yue, D.; Li, J.; Li, S. Numerical simulation and experimental study on shell inclination angle of classifier chamber in powder separator. *Coal Mine Mach.* **2009**, *30*, 49–51.

Disclaimer/Publisher's Note: The statements, opinions and data contained in all publications are solely those of the individual author(s) and contributor(s) and not of MDPI and/or the editor(s). MDPI and/or the editor(s) disclaim responsibility for any injury to people or property resulting from any ideas, methods, instructions or products referred to in the content.